AIAA SciTech Forum
23-27 January 2023, National Harbor, MD & Online
AIAA SCITECH 2023 Forum
10.2514/6.2023-0224

Further Refinement and Validation of the Spatially Filtered Wavefront Sensor as a Novel Aero-Optical Measurement Technique

Luke Butler[1], Stanislav Gordeyev[2]
University of Notre Dame, Notre Dame, IN, 46556

This paper validates the previously proposed concept of a spatially filtered wavefront sensor, which uses a convergent-divergent beam to reduce sensitivity to aero-optical distortions near the focal point while retaining sensitivity at regions with large beam diameters. This sensor was used to perform wavefront measurements in a cavity flow test section. The focal point was traversed to various spanwise locations across the test section, and the overall OPD_{RMS} levels and aperture-averaged spectra of wavefronts were computed. It was demonstrated that the sensor was able to effectively suppress the stronger aero-optical signal from the cavity flow and recover the weaker aero-optical signal from the boundary layer when the focal point was placed inside the shear region of the cavity flow. To model these measured quantities, additional collimated beam wavefronts were taken in a wind tunnel test section with two turbulent boundary layers, and then in the cavity flow test section, where the aero-optical signal from the cavity was dominant. The modelled results using the collimated data agree with the directly measured convergent-divergent beam results, confirming that the spatial filtering properties of the proposed sensor are due to attenuating effects at small apertures. Various techniques used to refine this sensor, allowing for a much better recovery of the cavity flow or boundary layer aero-optical spectra, are discussed.

I. Introduction

As a laser beam passes through turbulent flow, aero-optical structures of fluctuating densities impose optical aberration on the beam and, among other things, will cause the beam to propagate in a different direction. This is known as beam deflection or beam jitter. For small beam diameters, Huygens principle states [1] that the beam will be deflected by an amount proportional to the 2-D gradient of optical path length (OPL), according to

$$\theta_x(t) = \frac{\partial}{\partial x} OPL(x,y,t),\ \theta_y(t) = \frac{\partial}{\partial y} OPL(x,y,t)\,. \tag{1}$$

OPL, in turn, is an integral of the density field along the beam propagation, and is given by,

$$OPL(x,y,t) = K_{GD} \int \rho(x,y,z,t)\,dz\,, \tag{2}$$

where K_{GD} is Gladstone-Dale constant [1]. Thus, by projecting a single small-aperture laser beam through turbulent flows, wavefronts can be directly measured if the convective speed is known [2]. As wavefronts are proportional to the integrated density field, analysis of the time series of deflection angles informs knowledge of the underlying turbulent flow. This approach was

[1] Graduate student, Department of Aerospace and Mech. Eng., AIAA Student member.
[2] Associate Professor, Department of Aerospace and Mech. Eng., AIAA Associate Fellow

successfully used to study boundary layers [1,2,3], shear layers [1,4,5], and flows around turrets [6,7,8].

A wavefront sensor utilizes a high-speed camera with a lenslet array, along with a collimated laser beam in the area of interest and re-imaging lenses to place the image plane of the area of interest at the location of the lenslet array. The lenslet array focuses the laser light into many small airy disks, or spots, on the camera sensor, from which the centroids are computed at each moment in time. Based on the geometry of the lenslet array, the centroid displacements are converted to local deflection angles, and integration via e.g., Southwell's method [9] yields wavefronts. One challenge with this approach is that the measured wavefronts are line-of-sight integrated quantities. Thus, strong boundary layers and shocks often interfere with and mask the measurement of weaker signals of interest within the flow. For spanwise-uniform flows, this problem can be addressed by collecting wavefronts in both wall-normal and spanwise directions [10]. However, many flows of interest are not spanwise-uniform, or optical access may prevent multiple views.

The idea behind a Spatially Filtered Wavefront Sensor, or SFWFS, is that when piston and tip/tilt components are removed from wavefronts, the overall level of aero-optical distortion depends on the beam aperture size relative to a spatial scale of the flow [2,11]. A wavefront sensor using a converging-diverging beam should be less sensitive in the region near the focal point where the beam aperture is small, while the sensitivity is retained along the remainder of the beam. This can be useful for setups in which the laser beam goes through a region of interest and another region containing contaminating distortions, such as a boundary or shear layer near the tunnel wall.

Previous study has provided some basic proof-of-concept for the idea of a spatially filtered wavefront sensor to address this challenge [12]. However, there were many issues with these preliminary measurements which are either solved or addressed within this paper to further refine the technique. While the previous paper demonstrated qualitatively that attenuation could be attained using this technique, there were remaining discrepancies such as the absence of Rossiter modes and an amplitude mismatch across the spectra for the convergent-divergent data. These discrepancies are, for a large part, solved with more recent experiments, a more extensive comparison to expected values is performed, and sources for any remaining discrepancies are explained and discussed.

To demonstrate the spatial filtering ability of the convergent-divergent beam wavefront sensor, this technique was used to perform measurements in a test section with a turbulent boundary layer on one side and a cavity flow on the opposite wall. The dissimilar aero-optical environments of these flows allow for testing of the spatial filtering properties of this sensor. To quantify the aero-optical environment for each type of flow, separate collimated wavefront measurements were also performed in both the cavity flow test section and a test section with canonical boundary layers on both sides.

II. Experimental Setup

Experiments were performed using the 99x101 mm transonic in-draft wind tunnel at the Hessert Research Laboratory at the University of Notre Dame. The wind tunnel test sections have optical quality glass installed on the sides through which the laser beam is transmitted. A variable intensity 532 nm Nd:YAG laser was expanded to 25.4 mm using a beam collimator and, for the collimated experiments, further expanded to a 65 mm diameter using a -200 mm focal length lens followed by a 600 mm focal length lens, accounting for some cropping due to lens diameter. The setup for the collimated experiments is shown in Figure 1, while the setup for the convergent-divergent experiments is shown in Figure 2. Both setups used a Shack-Hartmann wavefront sensor, consisting of a Phantom v1611 high speed camera along with either a 40 mm or 38.2 mm focal length, 0.3 mm lenslet pitch, lenslet array. Data was acquired at a Mach number of 0.55.

Experiments were performed using a boundary layer test section that has turbulent boundary layers of δ=15.6 mm thickness on both walls, and a cavity flow test section which has a 15.6 mm boundary layer at one end and a cavity flow at the other. The streamwise length, *L*, of this cavity is 101.6 mm and the depth, *D*, is 25.4 mm. The cavity is located on the vertical wall of the test section, and the laser beam was transmitted through in the spanwise Y-direction, as shown in Figure 2. The cavity spans the entire spanwise Z-direction of the 99x101 mm test section.

For the collimated experiment, shown in Figure 1, a beam splitter was used to perform a double-pass experiment. The 65 mm return beam was contracted down to a 22 mm diameter through the beam cube and then re-imaged to a 17.4 mm beam on the sensor. Data was sampled at 25 kHz for both collimated and convergent-divergent beam experiments.

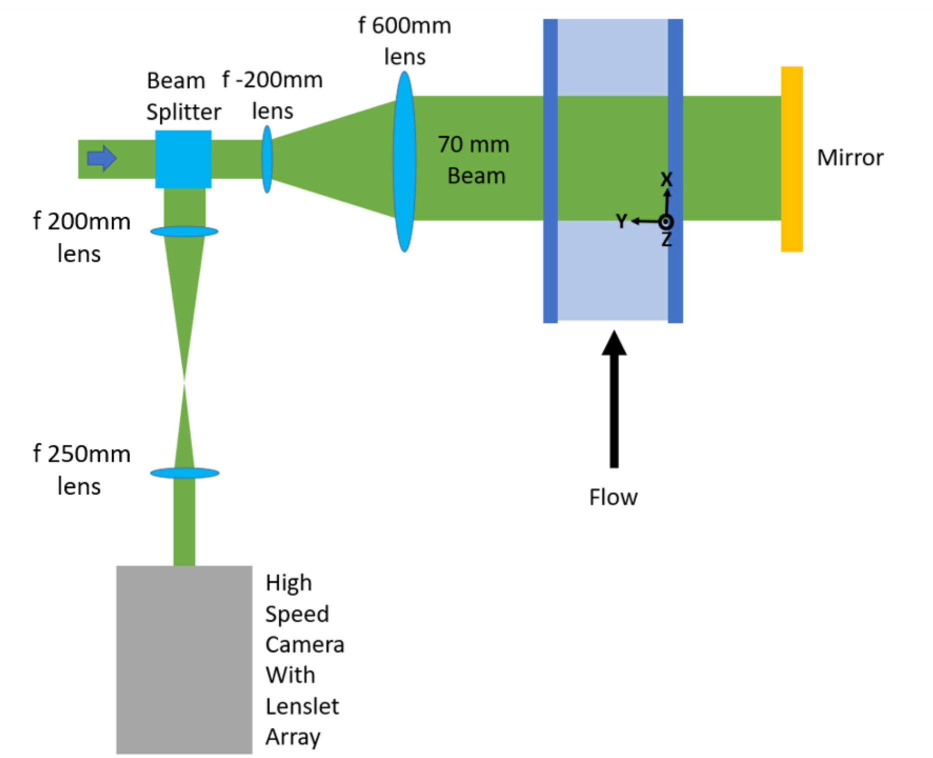

Fig. 1. Schematic of experimental setup for collimated wavefront boundary layer measurements. An f 250 lens followed by an f 200 lens is used for re-imaging, with 3.75x overall demagnification.

Figure 2 shows the schematic and a photo for the experimental setup with the convergent-divergent beam. Two 250 mm focal length lenses were placed at either side of the tunnel, such that the light converged to a focal point within the test section and was re-collimated thereafter. Using a pair of lenses, the outgoing beam was re-imaged onto a Shack-Hartmann wavefront sensor.

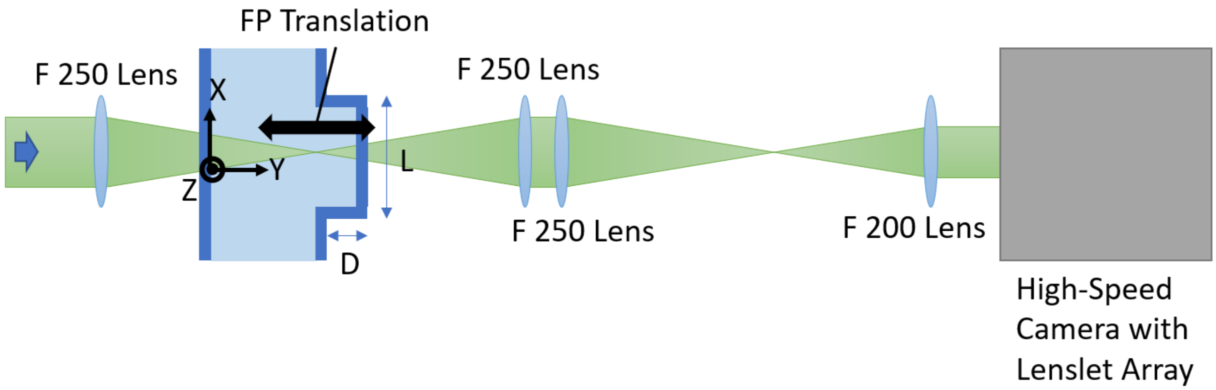

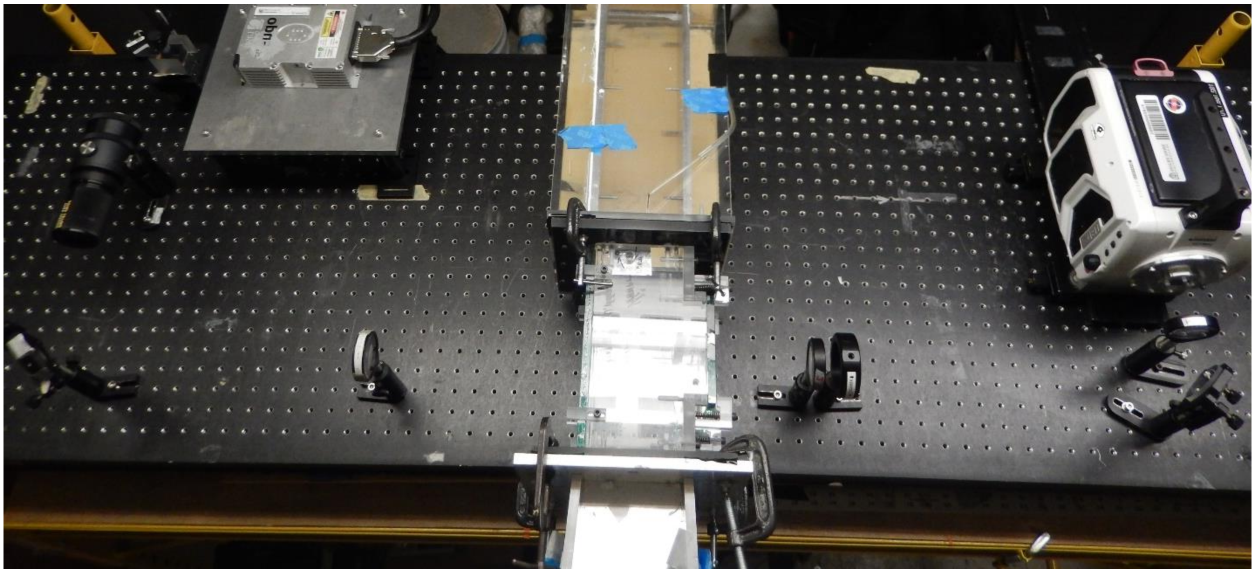

Fig. 2. Schematic and photo of experimental setup for convergent-divergent wavefront measurements in the cavity flow test section. Focal point can be translated to any Y-location within the test section.

In order to translate the focal point to various spanwise locations within the test section, the entire breadboard was placed on rails to allow for precise translation of the entire setup, as shown in Figure 3, to avoid any potential errors in beam alignment which could have been introduced if various portions of the setup were translated relative to each other. This translation apparatus also allowed for more rapid and precise collection of data.

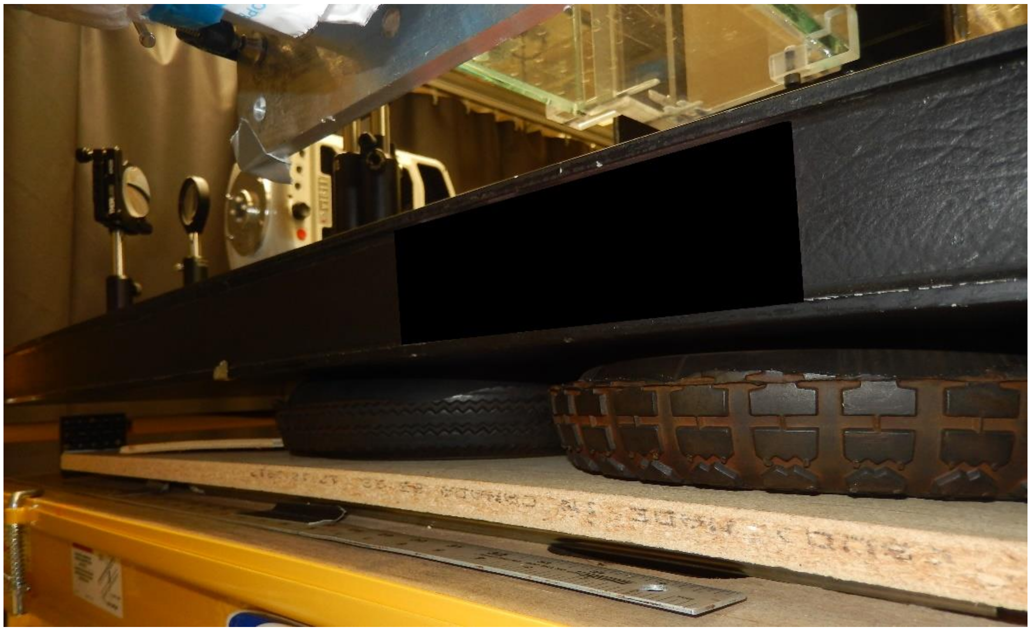

Fig. 3. Translation apparatus for entire experimental setup

III. Data Reduction

The lenslet array creates multiple focal spots on the camera sensor from which the spot centroids are extracted. Displacement of the centroids are converted to deflection angles by dividing by the lenslet focal distance of either 40 mm or 38.2 mm. Then, the Southwell method is used to integrate the deflection angles to yield wavefronts [9]. The global tip, tilt, and piston were removed from each wavefront by fitting and subtracting a plane at each timestep. Note that for all computations, two dimmer rows of boundary points were cropped before processing to retain the best quality data.

The aperture-averaged wavefront power spectra were computed using a standard block-averaging Fourier transform in time for each point and then averaging over all spatial points. The time-averaged root-mean-square optical path difference, or temporal OPD_{RMS}, was computed by taking the standard deviation over time for each spatial point in the wavefront data. The mean OPD_{RMS} was then computed by taking the average over all the points in the array.

IV. Results and Discussion

As the focal point was translated across the test section, various aperture sizes were present at the two flows of interest, the boundary layer on the far wall and the shear region of the cavity flow, set at the origin. Both were modeled as planes or phase screens for comparison with the collimated data. Once the aperture averaged wavefront power spectrum for each spanwise focal point location was computed, the corresponding aperture sizes at these two planes were used to obtain the contribution to the predicted power spectrum from each flow, and these two spectra were added together to obtain the modeled collimated result.

When the focal point is placed inside the optically weaker boundary layer flow, the cavity flow optical spectrum should be recovered, whereas when the focal point is placed inside shear region of the optically stronger cavity flow, the boundary layer optical spectrum should be reproduced. This is due to signals from any aero-optical structures larger than the beam aperture size being filtered out through the removal of tip/tilt, and the aperture at the focal point being essentially zero. In reality, there is some wall-normal thickness to the flows, which will introduce some error. Figure 4 (a) shows both the convergent-divergent and collimated spectra for when the focal point is in the boundary layer, while Figure 4 (b) shows these spectra for when the focal point is placed in the shear region of the cavity flow.

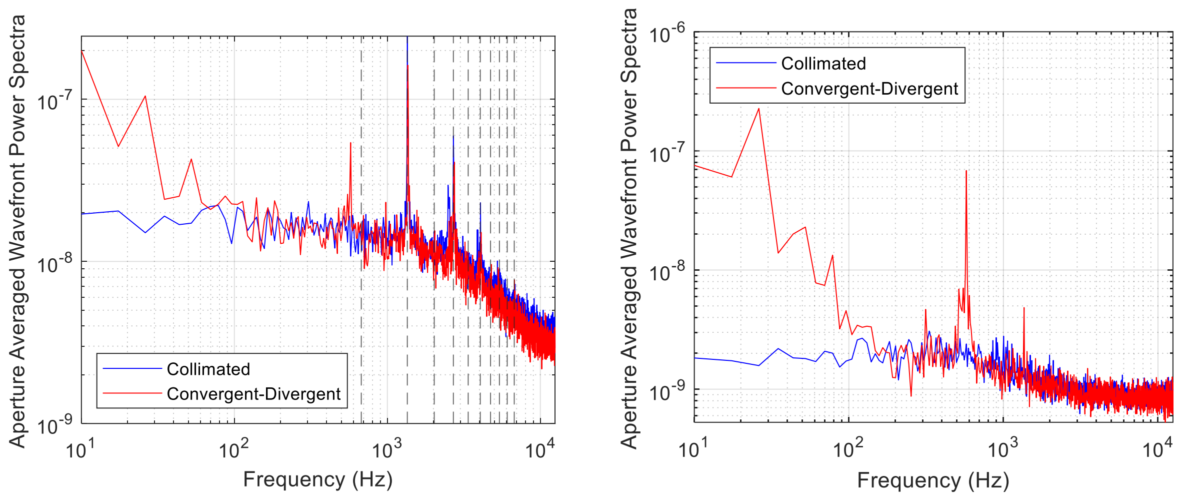

Fig. 4. Comparison between the spectra from the convergent-divergent beam and the modelled spectrum using the collimated data at Mach 0.55 for (a) with the focal point in the boundary layer and (b) with the focal point in the shear region of the cavity flow.

Cavity flows behave similarly to shear layers, with convecting structures corresponding to von Karman vortex shedding. The distance between minima in these structures Λ is 46.1 mm. The dashed vertical lines in Figure 4 (a) represent the expected Rossiter modes in the cavity, which are calculated using the equation below [13].

$$\frac{f_m L}{U_\infty} = \frac{m-\alpha}{\left[M_\infty\left(1+\frac{\gamma-1}{2}M_\infty\right)^{-1/2}+\frac{1}{\kappa}\right]} \quad (3)$$

Here, f_m is the Rossiter mode frequency, m is the mode number, L is the length of the cavity, equal to 0.1016 meters, U_∞ is the free stream velocity of 184.4 m/s, α is the phase lag, which was chosen to be zero, M_∞ is the Mach number of 0.55, γ is the ratio of specific heats of 1.4, and κ is the convective velocity, which is typically around 0.57 [14], but for this cavity flow was chosen to be 0.462 to align with the experimentally determined modes. Only even modes were excited.

The cavity flow spectrum in Figure 4 (a) closely aligns with the collimated data above 100 Hz, which is much better than the results from the preliminary studies in the previous paper, where the convergent-divergent spectrum was somewhat lower in amplitude than the collimated spectrum across most of the frequency range. Additionally, the Rossiter modes are recaptured, whereas they were not observed in the previous experiments. This shows that the current setup is able to obtain much cleaner data and is able to properly perform wavefront measurements of the flow, whereas in the previous measurements, although attenuation was demonstrated, wavefront measurements were not accurate enough to properly recreate the power spectrum. At both focal point locations, there is a spike just below 700 Hz. Additional investigation related this spike in the spectrum to air leakage detected along the wind tunnel, and not due to the flow of interest itself. The leakage will be fixed in future experiments, Figure 4 (b) shows that aside from this spike, the boundary layer spectrum from the convergent-divergent experiment almost perfectly matches the collimated spectrum, despite the presence of the optically-contaminating cavity flow around the focal point. A small peak from the first Rossiter mode is still detectable, but it is reduced by between 1 and 2 orders of magnitude when compared with the cavity flow at the same aperture. While either additional experiments at higher sampling frequency or with a wider beam could be able to recreate the full boundary layer spectrum at higher frequencies, the current results align almost perfectly despite both being optically aliased in a similar manner due to low sampling frequency. This shows that this technique is able to greatly attenuate much stronger aero-optical flows in order to recover much weaker aero-optical signals which would otherwise be obscured.

One source of contamination is the rise at low frequencies visible below 100 Hz. Ordinarily, in collimated wavefront measurements, mechanical vibrations are removed through the removal of tip/tilt. However, for the convergent-divergent beam, when the aperture is much smaller on the tunnel glass, any dust or other optical imperfections at or near the focal point get magnified, and can in effect amplify the effect of mechanical vibrations on the spectra. These imperfections are visible both on the camera, as shown in Figure 5, and in the wavefront movies. Future study may seek ways to remove this low frequency contamination if desired. This source of contamination may not be an issue where the contaminating flow is not near any tunnel glass, such as when optically mitigating a shear layer in an open-jet wind tunnel.

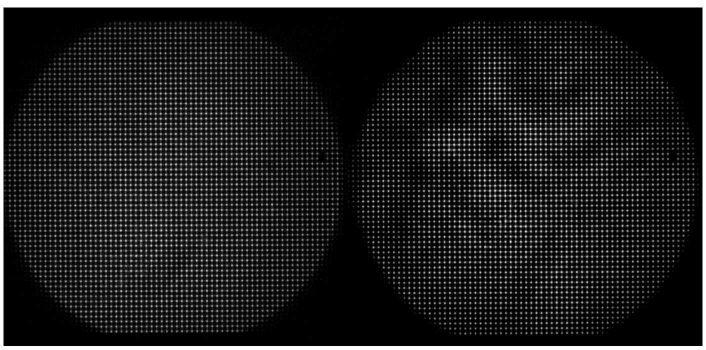

Fig. 5. Array of spots on camera sensor for clean collimated measurements (left) and convergent divergent measurements with dust and other imperfections magnified from areas of very small beam diameter (right).

Figure 6 shows the aperture-averaged wavefront power spectra for a spanwise sweep of the cavity flow test section at several focal point Y-locations across the tunnel. The vertical axis is the frequency, while the color hue represents the magnitude of the aperture averaged wavefront spectrum at that frequency. The boundary layer is located at the right edge and the origin was chosen to be in the center of the shear region of the cavity flow. Thus, due to attenuation near the focal point, the optically weaker boundary layer spectrum should be recovered at the origin and the optically stronger cavity flow spectrum should be recreated at the right edge. Figure 6 (a) shows the convergent-divergent beam sweep of the test section, while Figure 6 (b) shows the modelled results from the collimated data. The modelled results were calculated by adding the power spectra from each flow of interest with the proper aperture at each phase screen, as described earlier.

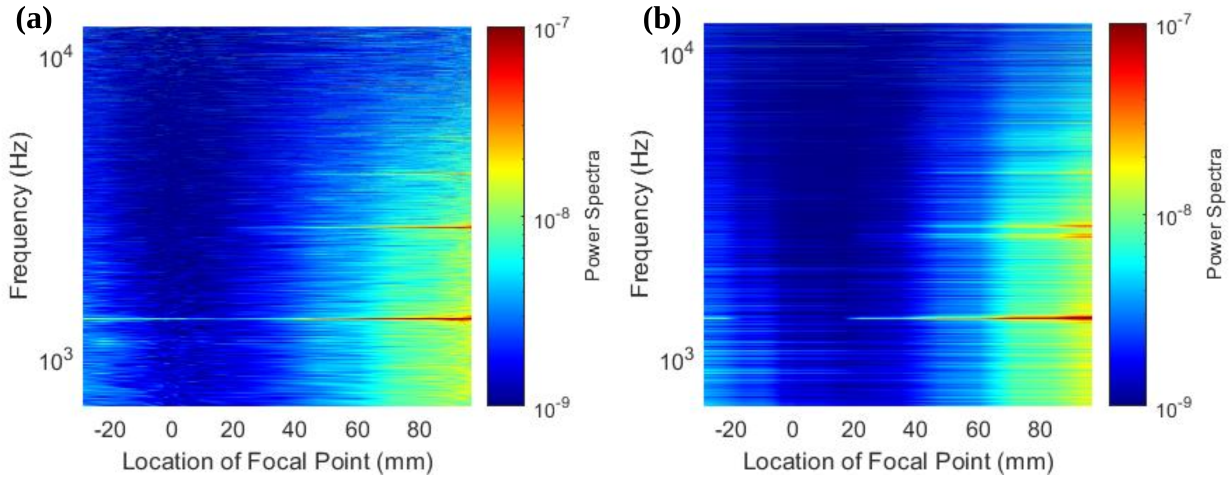

Fig. 6. Mach 0.55 spanwise sweep of cavity flow aperture-averaged wavefront spectra with the focal point at various Y-locations, (a) from convergent-divergent wavefront sensor, and (b) the modelled spectrum using the collimated data.

There is clearly significant attenuation present when the focal point is moved to the shear region, as expected, and the cavity flow spectrum along with peaks at the Rossiter modes is recreated when the focal point is moved to the boundary layer. There is a close resemblance between the convergent-divergent spectra and the expected spectra from the collimated measurements. Previous measurements were able to demonstrate attenuation, but did not recreate the spectra as well and only had faint, barely visible Rossiter modes, whereas the peaks in Figure 6 are clearly visible and are much greater in amplitude.

In addition to random noise, the main deviation from the modelled spectra occurs between around 20 and 40 mm, as is visible in Figure 7, which shows the normalized error in L_1-norm in the convergent-divergent spectra when compared with the collimated data, given by the Equation 4 below.

$$Error = \frac{|Convergent\text{-}Divergent - Collimated|}{Collimated} \tag{4}$$

This deviation between 20 and 40 mm is due to the cavity flow being approximated as a thin phase screen, when in reality, this flow has some spanwise width, which introduces additional contributions to the aero-optical spectra sooner than expected along the sweep of the test section. Then once the cavity flow becomes the main contributing factor to the spectra, the relative beam widths across it have smaller variation relative to the overall beam diameter, and this contributing error is once again mitigated when the focal point reaches the boundary layer.

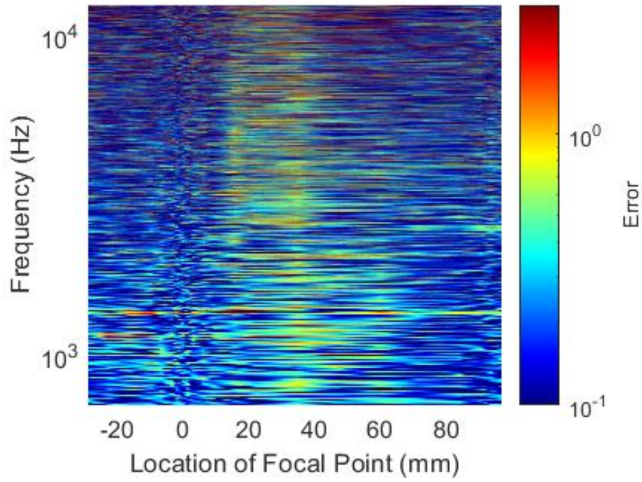

Fig. 7. Error in the convergent-divergent wavefront spectra from the sweep of the cavity flow at Mach 0.55 when compared with the modelling using the collimated beam data.

Assuming that the boundary layer and the cavity flow are statistically independent, the overall signal can be determined by the sum of the squares of OPD_{RMS}, similar to the procedure in [4], and given by,

$$OPD_{RMS} = \sqrt{OPD_{RMS,BL}^2 + OPD_{RMS,CAV}^2}. \tag{5}$$

There are two methods which can be used for computing OPD_{RMS} values from the wavefronts. One is to compute them from the wavefronts directly by computing the time-averaged OPD_{RMS} at each point across the aperture and then averaging over the aperture. Another method is by computing the OPD_{RMS} from the spectra, using Equation 6 below, where U_C is the convective velocity, selected to be $0.8U_\infty$, f is the frequency, $P_W(f)$ is the wavefront power spectrum, and f_c is the cutoff frequency, below which the contribution to the OPD_{RMS} is not computed to avoid low-frequency contamination,

$$OPD_{RMS} = \sqrt{2U_C \int_{f_C}^{\infty} \frac{P_W(f)df}{(2\pi f)^2}} \tag{6}$$

One issue with this method of OPD_{RMS} computation is that the magnitude relies heavily on the selected cutoff frequency, due to low frequencies contributing more to the OPD_{RMS}. However, one benefit with this method is that it allows for the elimination of the low frequency contamination discussed earlier. For both the convergent-divergent and the modeled results from collimated data, OPD_{RMS} values for the translation of the focal point across the tunnel at Mach 0.55 are presented in Figure 8, (a) using the spectral method with a cutoff frequency of 100 Hz, (b) using the spectral method with a cutoff frequency of 700 Hz, and (c) using the method of direct computation from wavefronts. Figure 8 (d) presents the error in the convergent-divergent data when compared with the collimated, once again computed by Equation 4, for each of these three computation methods.

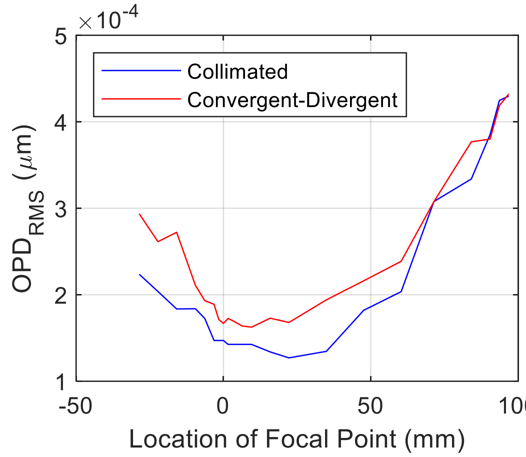

(a) Computed from Spectra, F_{cut} = 100 Hz

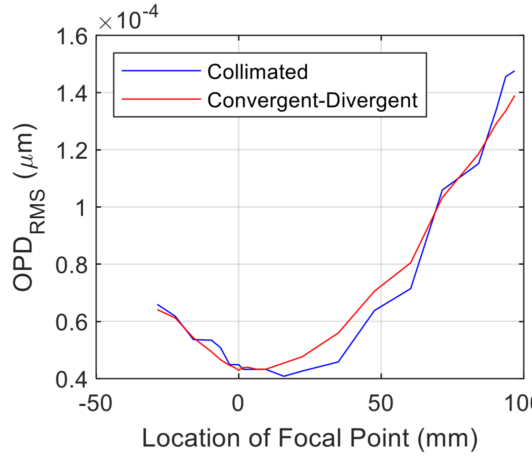

(b) Computed from Spectra, F_{cut} = 700 Hz

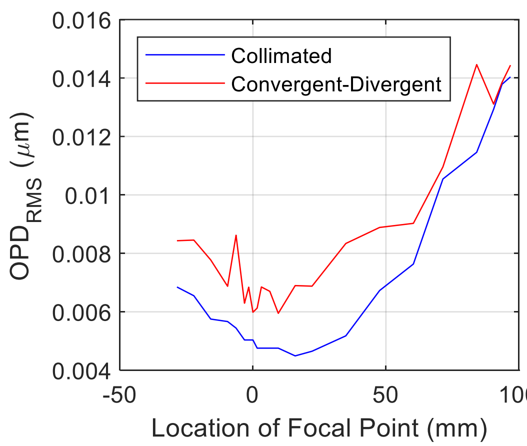

(c) Computed Directly from Wavefronts

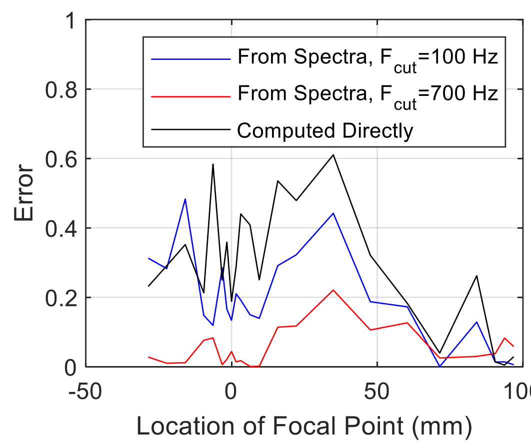

(d) Error when compared with Collimated

Fig. 8. OPD_{RMS} values as a function of the spanwise location of the focal point for the convergent-divergent beam at Mach 0.55, and with the modelled values computed using the collimated data, along with the computed errors from the collimated predictions.

Figure 8 (c) shows that the OPD_{RMS} values computed directly have the greatest discrepancy from the collimated results, while Figure 8(a) shows that getting rid of the low frequency noise rise below 100 Hz with the spectral method lessens this discrepancy somewhat. Figure 8(b) shows that by getting rid of the noise spike just below 700 Hz and any low frequency noise which may go above 100 Hz, the OPD_{RMS} values very closely match those from the modelled values using collimated measurements. One exception is when the focal point location is around the 15 to 60 mm mark, where there is a higher amplitude across the frequency range visible in Figure 7 and discussed earlier. Figure 8(d) shows that when the focal point is in the shear region of the cavity flow, the error in the OPD_{RMS} is around 30% when the OPD_{RMS} is calculated directly, around 20% using the spectral method with a cutoff frequency of 100 Hz, and around 5% when using the spectral method with a cutoff frequency of 700 Hz. This shows that apart from some low frequency discrepancies, the spatially filtered wavefront sensor is able to very closely recreate OPD_{RMS}

values from an optically weaker flow even when an optically stronger flow is present, which would normally obscure any measurements from a collimated wavefront sensor. However, one downside of the spectral method is that the amplitude is dependent on the cutoff frequency, so future studies may look into ways of getting rid of the mechanical vibrations due to magnification of dust and other optical imperfections, either through postprocessing or by avoiding having glass near areas where the beam diameter is small.

V. Conclusions

The concept of using a convergent-divergent beam to create a spatially filtered wavefront sensor with optical attenuation near the focal point, proposed previously in a preliminary study, was further refined and validated. This measurement technique relies on the fact that the filtering of tip, tilt, and piston components from wavefronts removes any aero-optical distortions larger than the aperture of the beam. As the beam aperture is almost zero near the focal point in a convergent-divergent beam, the contribution from the region near the focal point is removed, while the contributions from other regions are largely unaffected.

A demonstration was performed in a subsonic tunnel with two dissimilar aero-optical flows; a boundary layer at one tunnel wall and a flow over a cavity at the opposite wall. Wavefront data was collected with the focal point at various spanwise locations. In addition, collimated wavefront measurements were taken in the cavity flow test section and in a separate test section with boundary layers on either side. Using the collimated beam experiments, the wavefronts were re-apertured at progressively smaller apertures, and the aperture-related attenuating effect was confirmed in both the OPD_{RMS} levels and the spectra of aero-optical distortions.

Both spectral and OPD_{RMS} results from the convergent-divergent experiments matched the modeled values from collimated data much more closely than in the previous preliminary studies, with the spectra matching more closely over the whole frequency range in addition to the capturing of Rossiter modes, which were previously missed. Reasons for any remaining discrepancies, such as the low frequency mechanical vibration noise reintroduced from magnified dust and imperfections, were discussed. Future experiments could seek to eliminate or mitigate these discrepancies if desired, through either postprocessing or experimental design.

Most of the discrepancies between the collimated and convergent-divergent data present in the preliminary study presented earlier as a proof of concept were either eliminated or mitigated and explained in this paper, further validating the spatially filtered wavefront sensor as a viable non-intrusive aero-optical measurement technique with significant attenuation of any contaminating flow near the focal point along with the ability to closely recreate the spectra for any flow at beam locations with larger aperture. The SFWFS demonstrates the remarkable ability to perform correct measurements of much weaker optical flows which would otherwise be obscured by any stronger optically contaminating flows along the beam path for any conventional collimated wavefront measurements.

References

[1] S. Gordeyev, E.J. Jumper, “Physics and Measurement of Aero-Optical Effects: Past and Present,” Annual Review of Fluid Mechanics, **49**, pp. 419–441, 2017

[2] S. Gordeyev, A. E. Smith, J.A. Cress and E.J. Jumper, “Experimental studies of aero-optical properties of subsonic turbulent boundary layers," *Journal of Fluid Mechanics*, **740**, pp. 214-253, 2014.

[3] S. Gordeyev, J.A. Cress, A Smith and E.J. Jumper, " Aero-optical measurements in a subsonic, turbulent boundary layer with non-adiabatic walls", Physics of Fluids, 27, 045110, 2015.

[4] Malley M, Sutton GW, Kincheloe N. 1992. Beam-jitter measurements of turbulent aero optical path differences. Appl. Opt. 31:4440–43.

[5] Fitzgerald, E., and Jumper, E. (2004). The optical distortion mechanism in a nearly incompressible free shear layer. Journal of Fluid Mechanics, 512, 153-189.

[6] S. Gordeyev, T. Hayden and E. Jumper, "Aero-Optical and Flow Measurements Over a Flat-Windowed Turret", *AIAA Journal*, **45**(*2*), pp. 347-357, 2007.

[7] N. De Lucca, S. Gordeyev, and E. Jumper, "The Study of Aero-Optical and Mechanical Jitter for Flat-Windowed Turrets", AIAA Paper, 2012-0623.

[8] B. Vukasinovic, A. Glezer, S. Gordeyev, E. Jumper and V. Kibens, "Fluidic Control of a Turret Wake: Aerodynamic and Aero-Optical Effects", AIAA Journal, Vol. 48,No, 8, pp. 1686-1699, 2010.

[9] W. H. Southwell, "Wave-front estimation from wave-front slope measurements," Journal of the Optical Society of America, vol. 70, no. 8, pp. 998-1006, 1980.

[10] J. Sontag and S. Gordeyev, "Non-intrusive Velocity and Density Measurements in Subsonic Turbulent Boundary Layer ", AIAA Paper 2015-3247, 2015.

[11] Siegenthaler, J., “Guidelines for adaptive-optic correction based on aperture filtration,” PhD Thesis, University of Notre Dame, 2009.

[12] L.N. Butler, S. Gordeyev, K.P. Lynch and D. Guildenbecher, "Development of a Spatially Filtered Wavefront Sensor as an Aero-Optical Measurement Technique," AIAA AVIATION 2021 FORUM. August 2021, AIAA Paper 2021-3123.

[13] Wagner, J., Beresh, S.J., Casper, K.M., DeMauro, E.P., and Arunajatesan, S.. “Resonance Dynamics in Compressible Cavity Flows using Time-Resolved Particle Image Velocimetry and Pressure Sensitive Paint.” United States: N. p., 2017. Web. doi:10.2514/6.2017-0475.

[14] I. A. Zilberter and J. R. Edwards, “Numerical Simulation of Aero-Optical Effects in a Supersonic Cavity Flow” AIAA Journal, Vol. 55, No. 9, pp. 3096-3108, 2017.